The Astrophysical Journal Letters, 927:L19 (14pp), 2022 March 1 https://doi.org/10.3847/2041-8213/ac5823

Revisiting the Rates and Demographics of Tidal Disruption Events: Effects of the Disk Formation Efficiency

Thomas Hong Tsun Wong[1], Hugo Pfister[1,2], and Lixin Dai[1]
[1] Department of Physics, The University of Hong Kong Pokfulam Road, Hong Kong, People's Republic of China; twht@connect.hku.hk
[2] DARK, Niels Bohr Institute, University of Copenhagen Jagtvej 128, DK-2200 København, Denmark; lixindai@hku.hk
Received 2021 November 16; revised 2022 February 22; accepted 2022 February 24; published 2022 March 8

Abstract

Tidal disruption events (TDEs) are valuable probes of the demographics of supermassive black holes as well as the dynamics and population of stars in the centers of galaxies. In this Letter, we focus on studying how debris disk formation and circularization processes can impact the possibility of observing prompt flares in TDEs. First, we investigate how the efficiency of disk formation is determined by the key parameters, namely, the black hole mass $M_{\rm BH}$, the stellar mass $m_\star$, and the orbital penetration parameter β that quantifies how close the disrupted star would orbit around the black hole. Then we calculate the intrinsic differential TDE rate as a function of these three parameters. Combining these two results, we find that the rates of TDEs with prompt disk formation are significantly suppressed around lighter black holes, which provides a plausible explanation for why the observed TDE host black hole mass distribution peaks between 10^6 and $10^7\,M_\odot$. Therefore, the consideration of disk formation efficiency is crucial for recovering the intrinsic black hole demographics from TDEs. Furthermore, we find that the efficiency of the disk formation process also impacts the distributions of both stellar orbital penetration parameter and stellar mass observed in TDEs.

Unified Astronomy Thesaurus concepts: Tidal disruption (1696); High energy astrophysics (739); Supermassive black holes (1663); Black hole physics (159); Accretion (14); Galaxy accretion disks (562); Galaxy nuclei (609); Relativistic mechanics (1391); Stellar kinematics (1608); Stellar dynamics (1596)

1. Introduction

Stellar tidal disruption events (TDEs) occur whenever stars are gravitationally scattered into the vicinity of supermassive black holes (SMBHs) where tidal force dominates over the self-gravity of the stars (Rees 1988). This happens generally when the star enters the tidal disruption radius of the black hole (BH):

$$r_T \simeq \left(\eta^2 \frac{M_{\rm BH}}{m_\star}\right)^{1/3} r_\star, \tag{1}$$

where $M_{\rm BH}$ is the BH mass, and $m_\star$ and $r_\star$ are the mass and radius of the star. η is a parameter that depends on the details of the stellar structure (Ryu et al. 2020b; Law-Smith et al. 2020), and throughout this work, we take η to be unity for simplicity. After the disruption, approximately half of the stellar debris remains bound and forms an accretion disk, while the remaining stellar mass leaves the SMBH. When a sufficiently large fraction of the star is disrupted and accreted onto the BH, luminous flares can be produced through which we can peek into the event and its host SMBH (Guillochon & Ramirez-Ruiz 2013; Law-Smith et al. 2019).

The study of TDEs has inspired great interest, as these events can allow us to probe the vast majority of SMBHs, which are dormant. Moreover, it is shown that the observables of these events can be used to measure the BH mass, constrain the BH spin, as well as probe the stellar mass and structure (e.g., Kesden 2012; Mockler et al. 2019; Ryu et al. 2020a). Recently, this field has been growing fast not only because several dozens of TDE candidates have been detected in optical, UV, and X-ray wave bands (see reviews by Saxton et al. 2020; van Velzen et al. 2020; Gezari 2021), but also because thousands of TDEs are expected to be observed in the next decade using telescopes such as the Vera Rubin Observatory, eROSITA, and Einstein Probe. It will therefore be possible to use a large collection of TDEs to construct the demographics of massive BHs.

The rates of TDEs happening in galaxies with specific stellar density profiles can be calculated using the loss cone (LC) theory, which captures how two-body interactions can bring stars into low-angular-momentum orbits with pericenter within r_T (e.g., Merritt 2013). For example, Wang & Merritt (2004) apply the LC theory to two common galaxy density profiles and find that the TDE rate should be around $10^{-3}-10^{-4}\,{\rm gal}^{-1}\,{\rm yr}^{-1}$, which gradually decreases with increasing $M_{\rm BH}$. Stone & Metzger (2016) parameterize the observed galaxy samples with further consideration of stellar-mass functions and obtain a similar TDE rate dependency on $M_{\rm BH}$. This trend of decreasing TDE rates with increasing $M_{\rm BH}$ is seen again while taking into account nuclear star clusters in the center of dwarf galaxies (Pfister et al. 2020, 2022). The TDE rates also have a close correlation with the merger history (Pfister et al. 2019) and the structures of host galaxies (Law-Smith et al. 2019; French et al. 2020).

In summary, while the details depend somewhat on the stellar density profile and galaxy structure, the TDE rate of a galaxy should negatively correlate with $M_{\rm BH}$. Given there are more smaller galaxies hosting lighter BHs than the opposite (Reines & Volonteri 2015), we expect there should be more TDEs produced around lighter BHs. However, looking at the observed population of TDEs, one finds very few TDE candidates from BHs with $M_{\rm BH} \lesssim 10^5\,M_\odot$ (Wevers et al. 2017, 2019). Furthermore, Stone & Metzger (2016) and Hung et al. (2017) show that the TDE host $M_{\rm BH}$ distribution peaks between 10^6 and $10^7\,M_\odot$. This promotes the proposal that TDEs around more massive BHs have higher chances to be observed. Here we reexamine the observed TDE

Table A1
Chosen TDE Candidates with Their Host-galaxy Properties

Name	Redshift	σ (km s^{-1})	$\log_{10}\left(\frac{M_{\rm BH,\sigma}}{M_\odot}\right)$	$\log_{10}\left(\frac{M_{\rm gal}}{M_\odot}\right)$	$\log_{10}\left(\frac{M_{\rm BH,gal}}{M_\odot}\right)$	$\log_{10}(L_{\rm bb,peak}\,({\rm ergs}^{-1}))$
X-Ray TDEs						
2MASX J0249	0.0186	43^{+4}_{-4} [f]	$5.07^{+0.55}_{-0.62}$	$9.1^{+\dots}_{-\dots}$ [e]	$5.46^{+\dots}_{-\dots}$	…
2XMMi J1847–63	0.0353	…	…	…	…	$42.82^{+\dots}_{-\dots}$ [h]
3XMM J1500	0.1454	59^{+3}_{-3} [e]	$5.71^{+0.41}_{-0.45}$	$9.3^{+\dots}_{-\dots}$ [e]	$5.67^{+\dots}_{-\dots}$	$43.08^{+\dots}_{-\dots}$ [h]
3XMM J1521+0749	0.179	58^{+2}_{-2} [f]	$5.67^{+0.39}_{-0.41}$	$10.17^{+0.11}_{-0.20}$ [c]	$6.58^{+0.27}_{-0.40}$	$43.51^{+\dots}_{-\dots}$ [h]
ASASSN-14li	0.0206	81^{+2}_{-2} [b]	$6.35^{+0.30}_{-0.32}$	$9.71^{+0.05}_{-0.10}$ [g]	$6.10^{+0.26}_{-0.34}$	$43.66^{+0.02}_{-0.02}$ [g]
LEDA 095953	0.0366	…	…	…	…	…
NGC 5905	0.011	97^{+5}_{-5} [f]	$6.71^{+0.31}_{-0.35}$	$10.83^{+0.22}_{-0.06}$ [c]	$7.27^{+0.31}_{-0.17}$	$40.94^{+\dots}_{-\dots}$ [h]
RBS 1032	0.026	49^{+7}_{-7} [f]	$5.33^{+0.60}_{-0.71}$	$9.19^{+0.15}_{-0.16}$ [c]	$5.55^{+0.42}_{-0.47}$	$41.70^{+\dots}_{-\dots}$ [h]
RX J1242-1119-A	0.05	…	…	$10.3^{+\dots}_{-\dots}$ [e]	$6.72^{+\dots}_{-\dots}$	$42.60^{+\dots}_{-\dots}$ [h]
RX J1420+5334-A	0.147	131^{+13}_{-13} [f]	$7.32^{+0.33}_{-0.40}$	$10.53^{+0.07}_{-0.07}$ [c]	$6.96^{+0.19}_{-0.22}$	$43.38^{+\dots}_{-\dots}$ [h]
RX J1624+7554	0.0636	155^{+9}_{-9} [f]	$7.66^{+0.22}_{-0.26}$	$10.4^{+\dots}_{-\dots}$ [e]	$6.82^{+\dots}_{-\dots}$	$43.38^{+\dots}_{-\dots}$ [h]
SDSS J0159	0.3117	124^{+10}_{-10} [f]	$7.21^{+0.31}_{-0.36}$	$10.37^{+0.11}_{-0.06}$ [c]	$6.79^{+0.25}_{-0.22}$	…
SDSS J1201+3003	0.146	122^{+4}_{-4} [f]	$7.17^{+0.23}_{-0.25}$	$10.61^{+0.08}_{-0.16}$ [c]	$7.04^{+0.20}_{-0.31}$	$45.00^{+\dots}_{-\dots}$ [h]
SDSS J1311-0123	0.195	…	…	$8.7^{+\dots}_{-\dots}$ [f]	$5.04^{+\dots}_{-\dots}$	$41.74^{+\dots}_{-\dots}$ [h]
SDSS J1323+4827	0.0875	75^{+4}_{-4} [f]	$6.19^{+0.36}_{-0.40}$	$10.38^{+0.06}_{-0.07}$ [c]	$6.80^{+0.20}_{-0.23}$	$44.30^{+\dots}_{-\dots}$ [h]
Swift J1112	0.89	…	…	…	…	…
Swift J1644+57	0.3543	…	…	…	…	…
Swift J2058	1.186	…	…	…	…	…
TDXF J1347-32	0.0366	…	…	…	…	$42.73^{+\dots}_{-\dots}$ [h]
WINGS J1348+26	0.0651	…	…	$8.48^{+\dots}_{-\dots}$ [s]	$4.80^{+\dots}_{-\dots}$	$41.79^{+\dots}_{-\dots}$ [h]
XMM J0740	0.0173	…	…	…	…	$42.61^{+\dots}_{-\dots}$ [h]
Optical/UV TDEs						
ASASSN-14ae	0.044	53^{+2}_{-2} [f]	$5.49^{+0.41}_{-0.44}$	$9.73^{+0.13}_{-0.13}$ [c]	$6.12^{+0.34}_{-0.37}$	$43.87^{+0.01}_{-0.01}$ [g]
ASASSN-14li	0.0206	81^{+2}_{-2} [b]	$6.35^{+0.30}_{-0.32}$	$9.71^{+0.05}_{-0.10}$ [g]	$6.10^{+0.26}_{-0.34}$	$43.66^{+0.02}_{-0.02}$ [g]
ASASSN-15lh	0.233	225^{+15}_{-15} [d]	$8.41^{+0.16}_{-0.21}$	$10.8^{+\dots}_{-\dots}$ [d]	$7.24^{+\dots}_{-\dots}$	$45.6^{+\dots}_{-\dots}$ [d]
ASASSN-15oi	0.048	61^{+7}_{-7} [f]	$5.77^{+0.51}_{-0.60}$	$10.05^{+0.04}_{-0.04}$ [g]	$6.45^{+0.22}_{-0.23}$	$44.45^{+0.01}_{-0.01}$ [g]
ASASSN-19dj	0.022	…	…	$9.82^{+0.16}_{-0.13}$ [i]	$6.21^{+0.36}_{-0.36}$	$44.50^{+0.02}_{-0.02}$ [g]
AT 2018bsi	0.051	…	…	$10.63^{+0.05}_{-0.05}$ [i]	$7.06^{+0.17}_{-0.18}$	$43.87^{+0.08}_{-0.08}$ [g]
AT 2018dyb	0.018	96^{+1}_{-1} [s]	$6.69^{+0.24}_{-0.25}$	$9.86^{+0.08}_{-0.15}$ [g]	$6.25^{+0.28}_{-0.38}$	$44.08^{+\dots}_{-\dots}$ [h]
AT 2018dyk	0.037	112^{+4}_{-4} [f]	$7.00^{+0.25}_{-0.28}$	$10.6^{+\dots}_{-\dots}$ [f]	$7.03^{+\dots}_{-\dots}$	…
AT 2018hco	0.088	…	…	$9.95^{+0.12}_{-0.16}$ [i]	$6.35^{+0.31}_{-0.38}$	$44.25^{+0.04}_{-0.04}$ [g]
AT 2018hyz	0.0458	60^{+5}_{-5} [f]	$5.74^{+0.46}_{-0.52}$	$9.84^{+0.09}_{-0.14}$ [i]	$6.23^{+0.29}_{-0.37}$	$44.10^{+0.01}_{-0.01}$ [g]
AT 2018fyk	0.059	…	…	$10.58^{+0.12}_{-0.21}$ [g]	$7.01^{+0.24}_{-0.37}$	$44.48^{+\dots}_{-\dots}$ [h]
AT 2018iih	0.212	…	…	$10.63^{+0.18}_{-0.14}$ [i]	$7.06^{+0.29}_{-0.28}$	$44.62^{+0.04}_{-0.04}$ [g]
AT 2018lna	0.091	…	…	$9.49^{+0.11}_{-0.12}$ [i]	$5.86^{+0.35}_{-0.38}$	$44.56^{+0.06}_{-0.06}$ [g]
AT 2018lni	0.138	…	…	$10.00^{+0.09}_{-0.14}$ [i]	$6.40^{+0.27}_{-0.35}$	$44.21^{+0.29}_{-0.17}$ [g]
AT 2019ahk	0.0262	…	…	$9.72^{+0.09}_{-0.10}$ [g]	$6.11^{+0.30}_{-0.34}$	$44.08^{+\dots}_{-\dots}$ [h]
AT 2019bhf	0.1206	…	…	$10.25^{+0.14}_{-0.12}$ [i]	$6.66^{+0.30}_{-0.30}$	$43.91^{+0.04}_{-0.05}$ [g]
AT 2019cho	0.193	…	…	$10.20^{+0.11}_{-0.14}$ [i]	$6.61^{+0.27}_{-0.33}$	$43.98^{+0.01}_{-0.01}$ [g]
AT 2019dsg	0.0512	…	…	$10.46^{+0.11}_{-0.19}$ [i]	$6.88^{+0.25}_{-0.36}$	$44.26^{+0.04}_{-0.05}$ [g]
AT 2019ehz	0.074	…	…	$9.74^{+0.08}_{-0.09}$ [i]	$6.13^{+0.29}_{-0.33}$	$44.03^{+0.01}_{-0.02}$ [g]
AT 2019eve	0.064	…	…	$9.31^{+0.10}_{-0.15}$ [i]	$5.68^{+0.36}_{-0.44}$	$43.14^{+0.02}_{-0.03}$ [g]
AT 2019lwu	0.117	…	…	$9.86^{+0.09}_{-0.13}$ [i]	$6.25^{+0.29}_{-0.35}$	$43.60^{+0.03}_{-0.04}$ [g]
AT 2019meg	0.152	…	…	$9.70^{+0.15}_{-0.08}$ [i]	$6.09^{+0.36}_{-0.32}$	$44.36^{+0.03}_{-0.04}$ [g]
AT 2019mha	0.148	…	…	$10.07^{+0.10}_{-0.18}$ [i]	$6.47^{+0.28}_{-0.39}$	$44.05^{+0.06}_{-0.05}$ [g]
AT 2019qiz	0.0151	…	…	$10.01^{+0.09}_{-0.13}$ [i]	$6.41^{+0.27}_{-0.34}$	$43.44^{+0.01}_{-0.01}$ [g]
F01004	0.1178	132^{+29}_{-29} [f]	$7.33^{+0.51}_{-0.72}$	$9.8^{+\dots}_{-\dots}$ [f]	$6.19^{+\dots}_{-\dots}$	…
GALEX-D1-9	0.326	89^{+4}_{-4} [e]	$6.54^{+0.31}_{-0.35}$	$10.3^{+\dots}_{-\dots}$ [d]	$6.72^{+\dots}_{-\dots}$	$44.1^{+\dots}_{-\dots}$ [d]
GALEX-D23-H1	0.1855	84^{+4}_{-4} [f]	$6.42^{+0.33}_{-0.37}$	$10.08^{+0.15}_{-0.07}$ [c]	$6.48^{+0.33}_{-0.26}$	$43.9^{+\dots}_{-\dots}$ [d]
GALEX-D3-13	0.3698	133^{+6}_{-6} [f]	$7.35^{+0.23}_{-0.27}$	$10.7^{+\dots}_{-\dots}$ [c]	$7.14^{+\dots}_{-\dots}$	$44.3^{+\dots}_{-\dots}$ [d]
iPTF-15af	0.079	106^{+2}_{-2} [f]	$6.89^{+0.23}_{-0.25}$	$10.31^{+0.08}_{-0.10}$ [c]	$6.73^{+0.23}_{-0.28}$	$44.10^{+0.10}_{-0.08}$ [g]
iPTF-16axa	0.108	82^{+3}_{-3} [f]	$6.37^{+0.32}_{-0.35}$	$10.25^{+0.05}_{-0.08}$ [c]	$6.66^{+0.21}_{-0.25}$	$43.82^{+0.03}_{-0.02}$ [g]
OGLE16aaa	0.1655	…	…	$10.43^{+0.09}_{-0.11}$ [g]	$6.85^{+0.23}_{-0.27}$	$44.22^{+\dots}_{-\dots}$ [h]
PS1-10jh	0.1696	65^{+3}_{-3} [f]	$5.90^{+0.38}_{-0.42}$	$9.63^{+0.10}_{-0.13}$ [g]	$6.01^{+0.33}_{-0.38}$	$44.47^{+0.07}_{-0.07}$ [g]
PS16dtm	0.0804	45^{+13}_{-13} [f]	$5.16^{+0.84}_{-1.15}$	$9.77^{+0.11}_{-0.13}$ [c]	$6.16^{+0.32}_{-0.37}$	…

Table A1
(Continued)

Name	Redshift	σ (km s^{-1})	$\log_{10}\left(\frac{M_{\rm BH,\sigma}}{M_\odot}\right)$	$\log_{10}\left(\frac{M_{\rm gal}}{M_\odot}\right)$	$\log_{10}\left(\frac{M_{\rm BH,gal}}{M_\odot}\right)$	$\log_{10}(L_{\rm bb,peak}\,({\rm ergs}^{-1}))$
PS17dhz	0.1089	⋯	⋯	$9.47^{+0.11}_{-0.13}$ [g]	$5.84^{+0.36}_{-0.40}$	$43.82^{+\dots}_{-\dots}$ [h]
PS18kh	0.075	⋯	⋯	$9.95^{+0.12}_{-0.24}$ [i]	$6.35^{+0.31}_{-0.48}$	$43.78^{+0.02}_{-0.02}$ [g]
PTF-09axc	0.115	60^{+4}_{-4} [f]	$5.74^{+0.43}_{-0.48}$	$9.84^{+0.06}_{-0.09}$ [c]	$6.23^{+0.27}_{-0.31}$	$43.46^{+0.03}_{-0.02}$ [g]
PTF-09djl	0.184	64^{+7}_{-7} [f]	$5.87^{+0.49}_{-0.57}$	$9.91^{+0.13}_{-0.17}$ [c]	$6.31^{+0.32}_{-0.40}$	$44.42^{+0.04}_{-0.04}$ [g]
PTF-09ge	0.064	82^{+2}_{-2} [f]	$6.37^{+0.30}_{-0.32}$	$9.87^{+0.13}_{-0.17}$ [c]	$6.26^{+0.33}_{-0.40}$	$44.04^{+0.01}_{-0.01}$ [g]
PTF-10iya	0.224	⋯	⋯	$9.3^{+\dots}_{-\dots}$ [f]	$5.67^{+\dots}_{-\dots}$	⋯
SDSS-TDE1	0.136	126^{+7}_{-7} [b]	$7.24^{+0.26}_{-0.30}$	$10.08^{+0.08}_{-0.12}$ [c]	$6.48^{+0.26}_{-0.32}$	$43.5^{+\dots}_{-\dots}$ [d]
SDSS-TDE2	0.2515	⋯	⋯	$10.59^{+0.17}_{-0.10}$ [g]	$7.02^{+0.28}_{-0.24}$	$44.54^{+0.08}_{-0.06}$ [g]
SDSS J0748+4712	0.0615	126^{+7}_{-7} [f]	$7.24^{+0.26}_{-0.30}$	$10.18^{+0.06}_{-0.09}$ [c]	$6.59^{+0.23}_{-0.28}$	⋯
SDSS J0952+2143	0.0789	$95^{+\dots}_{-\dots}$ [a]	$6.67^{+\dots}_{-\dots}$	$10.37^{+0.06}_{-0.07}$ [c]	$6.79^{+0.20}_{-0.23}$	⋯
SDSS J1342+0530	0.0366	72^{+6}_{-6} [f]	$6.11^{+0.42}_{-0.48}$	$9.64^{+0.23}_{-0.07}$ [c]	$6.02^{+0.45}_{-0.31}$	⋯
SDSS J1350+2916	0.0777	⋯	⋯	$9.94^{+0.17}_{-0.20}$ [c]	$6.34^{+0.35}_{-0.43}$	⋯

Notes. The columns are TDE name, redshift, velocity dispersion σ, black hole mass $M_{\rm BH,\sigma}$ derived from the $M_{\rm BH}-\sigma$ relation, galaxy stellar mass $M_{\rm gal}$, black hole mass $M_{\rm BH,gal}$ derived from the $M_{\rm BH}-M_{\rm gal}$ relation, and peak luminosity assuming blackbody emission $L_{\rm bb,peak}$. The chosen TDEs are separated into either the optical/UV-strong or X-ray-strong categories, except for ASASSN-14li, which is in both categories. References for the values of σ, $M_{\rm gal}$, and $L_{\rm bb,peak}$:
[a] Komossa et al. (2008),
[b] Wevers et al. (2017),
[c] Graur et al. (2018),
[d] van Velzen (2018),
[e] Wevers et al. (2019),
[f] French et al. (2020),
[g] van Velzen et al. (2020),
[h] Gezari (2021),
[i] van Velzen et al. (2021),
[s] Source discovery papers. Their 1σ error bars of $M_{\rm BH}$ are calculated by modeling each TDE as a Gaussian distribution with the scattering from the $M_{\rm BH}$-scaling relations and the measurement errors from σ and $M_{\rm gal}$.

$M_{\rm BH}$ distribution given that the sample size has grown significantly in the past few years. We refer to several recent reviews and pick out a total of 65 likely TDE candidates (the selection criteria are detailed in Appendix A). We also calculate their $M_{\rm BH}$ consistently using two different methods: $M_{\rm BH}-\sigma$ (Merritt & Ferrarese 2001) and $M_{\rm BH}-M_{\rm gal}$ (Reines & Volonteri 2015). The full list of selected TDE candidates and their $M_{\rm BH}$ is shown in Table A1. We show the normalized distribution of $M_{\rm BH}$ for these observed TDEs in Figure 1. The distributions for both TDE lists still center around 10^6–$10^7\,M_\odot$ and drop off toward both ends of the mass spectrum, regardless of the methods used to derive $M_{\rm BH}$. In the same figure, we also show the theoretically computed TDE $M_{\rm BH}$ distribution from the LC dynamics (see Appendix C for detailed calculations) for comparison, where one sees an increasing TDE rate with decreasing $M_{\rm BH}$.

The large discrepancy between the intrinsic and observed TDE $M_{\rm BH}$ distribution can result from many factors such as survey constraints and dusts (van Velzen 2018; Roth et al. 2021). Also, the disk formation, accretion, and emission processes in TDEs (Roth et al. 2020; Bonnerot & Stone 2021; Dai et al. 2021, respectively) can play a major role in altering the observed TDE $M_{\rm BH}$ distribution. One possible explanation is that the TDE luminosity is capped at the Eddington luminosity limit and therefore scales with $M_{\rm BH}$ (Kochanek 2016). However, the peak luminosity of the observed TDE candidates does not show any clear linear trend with the host $M_{\rm BH}$ (Figure A2). Although we cannot rule out the Eddington-limit model due to possible observational biases and the limited dynamic range of the data, we turn our focus to the disk formation process because recent hydrodynamics simulations show that not all TDEs can form circular disks efficiently through stream self-crossings (see review by Bonnerot & Stone 2021). In particular, Shiokawa et al. (2015) show that in the case of inefficient disk circularization, accretion onto SMBHs will happen on timescales much longer than the fallback timescale, which can lower the possibility of the detection of such events. Based on these simulations, Dai et al. (2015) and Guillochon & Ramirez-Ruiz (2015) use first-order calculations to quantify how the disk formation promptness depends on the BH mass and stellar orbital parameters. It is found that in TDEs around more massive BHs the stream self-crossings are closer to the BH due to stronger general relativistic (GR) effects. The closer self-crossings give stronger collisions, leading to faster disk formation and accretion and more prompt flares. Therefore, the disk formation process is a natural candidate for a mechanism that can promote TDEs around more massive SMBHs to be observed.

In this paper, we aim at mitigating the TDE $M_{\rm BH}$ distribution tension from the perspective of disk formation efficiency. We hypothesize that inefficient disk circularization processes significantly reduce the chance of TDEs being detected around lighter SMBHs. Using the first-order framework of Dai et al. (2015), we further quantify the disk formation efficiency as a function of key parameters (Section 2). Next we obtain the differential TDE rates from the LC theory and check how including the correction by the disk formation efficiency can shift the TDE $M_{\rm BH}$ distribution (Section 3). Then, we reexamine the distributions of some key parameters in TDEs (Section 4). Lastly, a summary and further discussions are given (Section 5).

2. Efficiency of Disk Formation from Debris Stream Self-crossing

Recent studies have consistently shown that the formation of TDE disks is mainly caused by the self-crossing of the debris

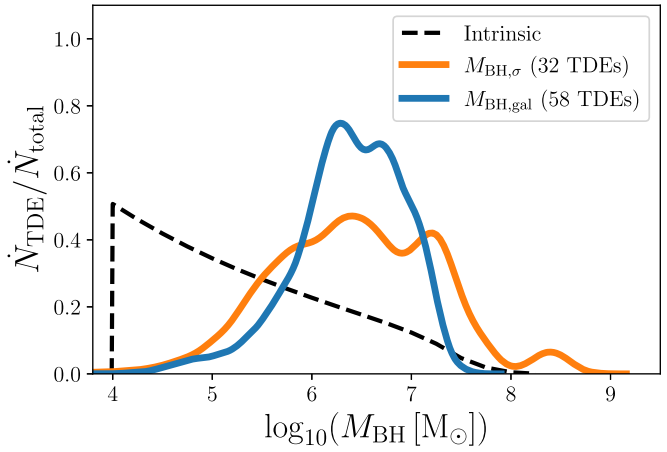

Figure 1. The host $M_{\rm BH}$ distribution of the observed TDE candidates compared to the intrinsic distribution from the LC theory. The solid lines represent our chosen observed TDE candidates, while the colors indicate the methods used to constrain $M_{\rm BH}$ (orange: $M_{\rm BH}$–σ; blue: $M_{\rm BH}$–$M_{\rm gal}$). Similar to the bootstrapping method, the error bars of individual TDEs are modeled as a Gaussian distribution with the scattering from the $M_{\rm BH}$-scaling relations and the measurement errors from σ and $M_{\rm gal}$. Both observed TDE $M_{\rm BH}$ distributions center around 10^6–$10^7\,M_\odot$, while the intrinsic TDE $M_{\rm BH}$ distribution derived from the LC dynamics (black dashed curve) peaks toward lighter BHs. The small peak of the orange curve at 10^8–$10^9\,M_\odot$ is due to a single event ASASSN-15lh.

stream due to GR apsidal precession near SMBHs. Some fraction of the stellar debris becomes unbound due to shocks, while the remaining rapidly dissipates its orbital energy to form a somewhat circular accretion disk, generally within a few orbital timescales (Lu & Bonnerot 2020). For stars disrupted along inclined orbits around spinning BHs, Lense–Thirring precession can complicate the process (Kochanek 1994; Dai et al. 2013; Guillochon & Ramirez-Ruiz 2015), although the latest hydrodynamical simulations show that disks still form after a short delay (Liptai et al. 2019). Despite these advancements, full-scale simulations of complex disk formation processes are still not achieved due to computational limitations.

In this study, we follow the first-order calculations in Dai et al. (2015) for debris dynamics and kinematics around a Schwarzschild BH. The basics are detailed in Appendix B. Starting from there, the specific energy loss at the self-crossing point R_I is approximated as

$$\Delta E_{\rm first} = \left| \frac{1}{2}v_f^2 - \frac{1}{2}v_i^2 \right|, \tag{2}$$

where v_f and v_i are the debris speeds before and after collision respectively. The bound debris has to lose a significant amount of orbital energy, likely through the shocks and dissipation happening in repeated self-crossings in order to form a disk. In theory, if the debris could completely circularize, the classical circularization radius can be calculated using the conservation of angular momentum:

$$r_{\rm circ} = \frac{2r_T}{\beta}, \tag{3}$$

where $\beta = r_T/r_p$ is the penetration parameter quantifying how deeply the star plunges into the BH gravitational potential well. Therefore, the total specific orbital energy needed to be removed from the initially elliptical orbit for complete circularization is

$$\begin{aligned}\Delta E_{\rm total} &= E_{\rm ellip} - E_{\rm circ} \\ &= -\frac{GM_{\rm BH}}{2a_{\rm mb}} + \frac{GM_{\rm BH}}{2r_{\rm circ}} \\ &= \frac{GM_{\rm BH}}{2}\left(\frac{\beta}{2r_T} - \frac{1}{a_{\rm mb}}\right),\end{aligned} \tag{4}$$

where $a_{\rm mb}$ is the semimajor axis of the most bound debris orbit. (Strictly speaking, the debris falling back at the peak of the flare should be slightly less bound than the most bound debris. Therefore, the $\Delta E_{\rm total}$ obtained here is a lower limit.)

Given that the subsequent collisions and interactions after the first debris self-crossing are hard to trace analytically, we define a first-order, dimensionless disk formation (circularization) efficiency parameter by scaling Equation (2) with Equation (4):

$$\mathcal{C}(M_{\rm BH}, \beta, m_\star) \equiv \frac{\Delta E_{\rm first}}{\Delta E_{\rm total}}. \tag{5}$$

When $\mathcal{C} \ll 1$, the debris stream self-crossing happens far away from the BH and the disk formation is expected to be slow, which lowers the possibility of detecting prompt flares from such events. On the other hand, when $\mathcal{C} \sim 1$, the debris can already dissipate a large fraction of its orbital energy through the shocks at the first self-crossing, and we expect such TDEs will likely produce prompt, observable flares.

The tidal radius r_T can be expressed as a function of only $M_{\rm BH}$ and $m_\star$ for main-sequence (MS) stars because their masses and radii are linked by Kippenhahn & Weigert (1990) as

$$\frac{r_\star}{R_\odot} = \begin{cases} \left(\dfrac{m_\star}{M_\odot}\right)^{0.8} & \text{for } m_\star \leqslant M_\odot \\ \left(\dfrac{m_\star}{M_\odot}\right)^{0.57} & \text{for } m_\star \geqslant M_\odot \end{cases}. \tag{6}$$

Therefore, $\mathcal{C}$ can be expressed as a function of three parameters: $M_{\rm BH}$, $m_\star$, and β. We plot the values of $\mathcal{C}$ as contour lines in the left column of Figure 2 for three representative $M_{\rm BH}$. One can see that for intermediate-mass black holes (IMBHs) with $M_{\rm BH} \sim 10^4\,M_\odot$, extremely large $\beta >$ few $\times$ 10 will be needed for having efficient disk formation. For $M_{\rm BH} \sim 10^6\,M_\odot$, low-mass, denser stars with $m_\star \sim 0.1\,M_\odot$ can have moderately prompt disk formation for all β, while for more massive stars the disk formation is slow unless $\beta >$ a few. For very massive black holes with $M_{\rm BH} \sim 10^8\,M_\odot$, the disk formation is always efficient, but only stars with $m_\star \gtrsim 1\,M_\odot$ can still be disrupted outside the BH event horizon.

In the subsequent sections, we apply the $\mathcal{C}$-correction to the observed TDE rates and demographics in two different ways: one way is to directly use $\mathcal{C}$ as the probability of observing an event $P_{\rm obs}$, the other way is that we pick a particular threshold value $\mathcal{C}_{\rm thres}$ to screen out TDEs with $\mathcal{C} < \mathcal{C}_{\rm thres}$. For the latter, reasonable choices of $\mathcal{C}_{\rm thres}$ can be obtained by comparing the TDE light-curve decay timescale ($\sim$1 yr for typical parameters) and the orbital timescale of the most bound orbit ($T_{\rm mb} \sim 1$ month for typical parameters). The timescale to circularize the elliptical orbit is approximately $T_{\rm circ} = nT_{\rm mb}$, where n is the number of stream self-crossings (Ulmer 1998). For the dynamical fallback pattern to

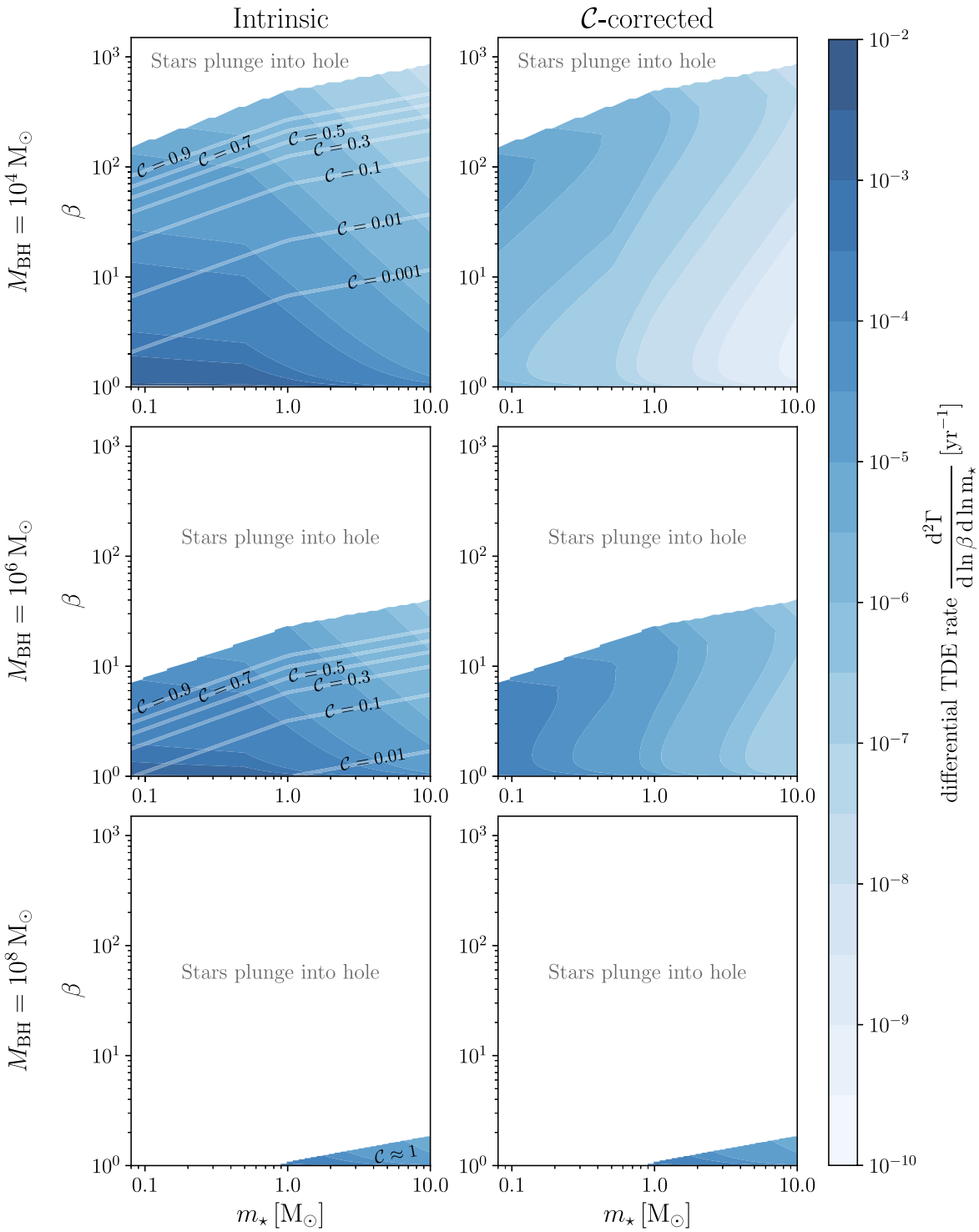

Figure 2. Comparison between the intrinsic and $\mathcal{C}$-corrected differential TDE rates. For $M_{\rm BH}/M_\odot = \{10^4, 10^6, 10^8\}$ (top, middle, and bottom rows), the intrinsic and corrected differential TDE rates are shown in the left and right panels, respectively. The white regions represent the parameter space where stars directly plunge into the BH event horizon. Contours of disk formation efficiencies $\mathcal{C}$ are overplotted in the left panels. $\mathcal{C}$ has a monotonically increasing trend toward the upper-left corner (higher β and lower $m_\star$). One can see that the $\mathcal{C}$-correction leads to a significant drop in TDE rates at low β for lighter BHs. For $M_{\rm BH} = 10^8\,M_\odot$, $\mathcal{C} \approx 1$ across the TDE-allowed parameter space.

be reserved, the disk formation should in principle happen faster than the fallback timescale, which gives $n \lesssim 10$ and $\mathcal{C}_{\rm thres} \sim 1/n \gtrsim 0.1$.

We also note that there are ongoing discussions on whether the optical emissions from TDEs are powered by accretion or the shocks induced in the debris self-crossing (e.g., Piran et al. 2015; Bonnerot & Lu 2020). Nonetheless, the chance of observing a particular TDE flare, even if only powered by debris self-crossing, should still have a tight correlation with $\Delta E_{\rm first}$. Therefore, the correction between the observed TDE

rates and $\mathcal{C}$ should hold regardless of the origin of TDE optical emissions, which awaits to be disclosed by further studies.

3. Revised TDE Rates

3.1. Intrinsic TDE Rates from Loss Cone Dynamics

We apply the LC theory and calculate the TDE rates. In this work, we only consider bright TDE flares from full disruption scenarios because it is hard to distinguish whether a dim flare is produced due to slow disk formation or partial disruption. We refer the readers to Pfister et al. (2022) for the calculations used in this work, which we also include in Appendix C for completeness.

Assuming the Kroupa stellar-mass function (Kroupa 2001), an isothermal stellar density profile ($\rho \propto r^{-2}$), and the BH mass following the $M_{\rm BH}-\sigma$ relation (Merritt & Ferrarese 2001), the intrinsic differential TDE rate can be analytically computed as a function of $M_{\rm BH}$, $m_\star$, and β (Pfister et al. 2022):

$$\frac{d^2\Gamma}{d\ln\beta\, d\ln m_\star} = \frac{8\pi^2 G M_{\rm BH} r_T}{\beta}\phi(m_\star)m_\star \times \int_0^{GM_{\rm BH}/r_T} \mathcal{G}(E, M_{\rm BH}, \beta, m_\star)dE, \quad (7)$$

where $\phi(m_\star)$ is the Kroupa stellar-mass function and $\mathcal{G}(E, M_{\rm BH}, \beta, m_\star)$ is a complex function that gathers the essence of the LC dynamics.

Under this simplified framework, we vary $M_{\rm BH}$ in the range $[10^4\,M_\odot, 10^9\,M_\odot]$ while bearing in mind the existence of IMBHs is still under debate. We include the MS stars in the range of $[0.08\,M_\odot, 10\,M_\odot]$. The penetration parameter β varies between 1 and $\beta_{\rm max}$, where $\beta_{\rm max} = r_T/2r_g$ corresponds to the orbit with r_p at the BH Schwarzschild radius. For a fixed $M_{\rm BH}$, $\beta_{\rm max}$ is set by the most massive star, so we have $\beta_{\rm max}^{10\,M_\odot} = \beta_{\rm max}(M_{\rm BH}, 10\,M_\odot)$, which has a value of $\sim 10^3$ when $M_{\rm BH} = 10^4\,M_\odot$, ~ 40 when $M_{\rm BH} = 10^6\,M_\odot$, and ~ 1 when $M_{\rm BH} = 10^8\,M_\odot$. We show the intrinsic differential TDE rate in Figure 2 (left panels). This plot depicts that most TDEs have $\beta \sim 1$, and most disrupted stars have low masses unless for $M_{\rm BH} \gtrsim 10^8\,M_\odot$.

3.2. Corrected TDE Rates with Disk Formation Efficiency

Following the discussion in Section 2, we multiply the intrinsic differential TDE rates (Equation (7)) with the disk formation efficiency parameter $\mathcal{C}$ to obtain the predicted observed differential TDE rates:

$$\frac{d^2\Gamma_{\mathcal{C}}}{d\ln\beta\, d\ln m_\star} \equiv \mathcal{C} \times \frac{d^2\Gamma}{d\ln\beta\, d\ln m_\star}, \quad (8)$$

where Γ and $\Gamma_{\mathcal{C}}$ stand for the intrinsic and $\mathcal{C}$-corrected rates, respectively. $\Gamma_{\mathcal{C}}$, as a function of β and $m_\star$, is shown in Figure 2 (right panels). Comparing the two rates, the most notable difference is that the β-distribution becomes much more even for the same $m_\star$ after the $\mathcal{C}$ correction. This is because the substantial reduction of the TDE rates mostly happens at low β due to small $\mathcal{C}$, where the intrinsic rate is large. Also, $\Gamma_{\mathcal{C}}$ has a more sensitive dependence on $m_\star$, which results from larger stars, which are rare, initially also generally having smaller $\mathcal{C}$ values. However, for $M_{\rm BH} \approx 10^8\,M_\odot$, $\mathcal{C} \approx 1$, so the rates and distributions are barely altered.

3.3. TDE Host Black Hole Mass Distribution

The volumetric TDE rates as a function of the host BH mass can be obtained with the results above and the information on the BH mass function (BHMF). The BHMF $\Phi_{\rm BH}$, defined as the number of SMBHs per comoving volume between masses $M_{\rm BH}$ and $M_{\rm BH} + dM_{\rm BH}$, provides knowledge on the growth and evolution of SMBHs and galaxies. Currently, the observationally constrained BHMF still has a large uncertainty (e.g., Shankar et al. 2016; Gallo & Sesana 2019). In particular, the uncertainty in BH occupation fraction increases significantly toward lighter BHs of $M_{\rm BH} \lesssim 10^5\,M_\odot$, which also results in the uncertainty of TDE rates around such BHs. We have shown in Appendix D that the uncertainty in the moderately constrained BHMF at the low-mass end is insufficient to explain the TDE BH mass distribution as observed.

In this work, we adopt the BHMF $\Phi_{\rm BH}$ derived by Gallo & Sesana (2019):[3]

$$\log_{10}\left(\frac{\Phi_{\rm BH}}{\rm Mpc^{-3}\,M_\odot^{-1}}\right) = -9.82 - 1.10 \times \log_{10}\left(\frac{M_{\rm BH}}{10^7\,M_\odot}\right) - \left(\frac{M_{\rm BH}}{128 \times 10^7\,M_\odot}\right)^{1/\ln(10)}, \quad (9)$$

which constrains the local SMBH occupation fraction and incorporates the latest galaxy stellar-mass function with Chandra X-ray data. Most importantly, this BHMF takes into account the nonunity SMBH occupation fraction in galaxies toward the near-IMBH mass spectrum. Furthermore, because all TDE candidates discovered so far are at low redshifts $z \sim 0.01$–0.4, this particular BHMF derived from the local SMBHs is applicable for this redshift range.

The predicted volumetric intrinsic and $\mathcal{C}$-corrected TDE rates are, respectively,

$$\dot{n}(M_{\rm BH}) = \Phi_{\rm BH} \times \int\left(\frac{d^2\Gamma}{d\ln\beta\, d\ln m_\star}\right) d\ln\beta\, d\ln m_\star, \quad (10a)$$

$$\dot{n}_{\mathcal{C}}(M_{\rm BH}) = \Phi_{\rm BH} \times \int\left(\frac{d^2\Gamma_{\mathcal{C}}}{d\ln\beta\, d\ln m_\star}\right), \quad (10b)$$
$$d\ln\beta\, d\ln m_\star$$

which are plotted in Figure 3(a). The integrated volumetric rate of all $M_{\rm BH}$ is $\lesssim 10^{-5}\,{\rm Mpc^{-3}\,yr^{-1}}$ for $\mathcal{C}_{\rm thres} \gtrsim 0.1$, which lies a little beyond the TDE rate inferred from current observations, $\dot{n} \approx 4 \times 10^{-8.4} - 5.4 \times 10^{-6}\,{\rm Mpc^{-3}\,yr^{-1}}$ (Stone et al. 2020 and references therein). This could result from the isothermal stellar density profile used in our calculation, the BHMF uncertainty at low $M_{\rm BH}$, and observational limitations. Therefore, we check how the normalized TDE $M_{\rm BH}$ distribution changes after considering the disk formation efficiency in Figure 3(b), which depends less on various assumptions. Similar to the rates, after applying the $\mathcal{C}$ corrections, the $M_{\rm BH}$ distribution shifts toward the more massive side of the spectrum and peaks around 10^6–$10^7\,M_\odot$.

Suppose that the disk formation efficiency is the sole mechanism affecting the observed $M_{\rm BH}$ distribution, we find $\mathcal{C}_{\rm thres} \approx 0.1$ would give the best-fit distribution according to the

[3] The equation is the corrected version of Gallo & Sesana (2019), reported in Pfister et al. (2022).

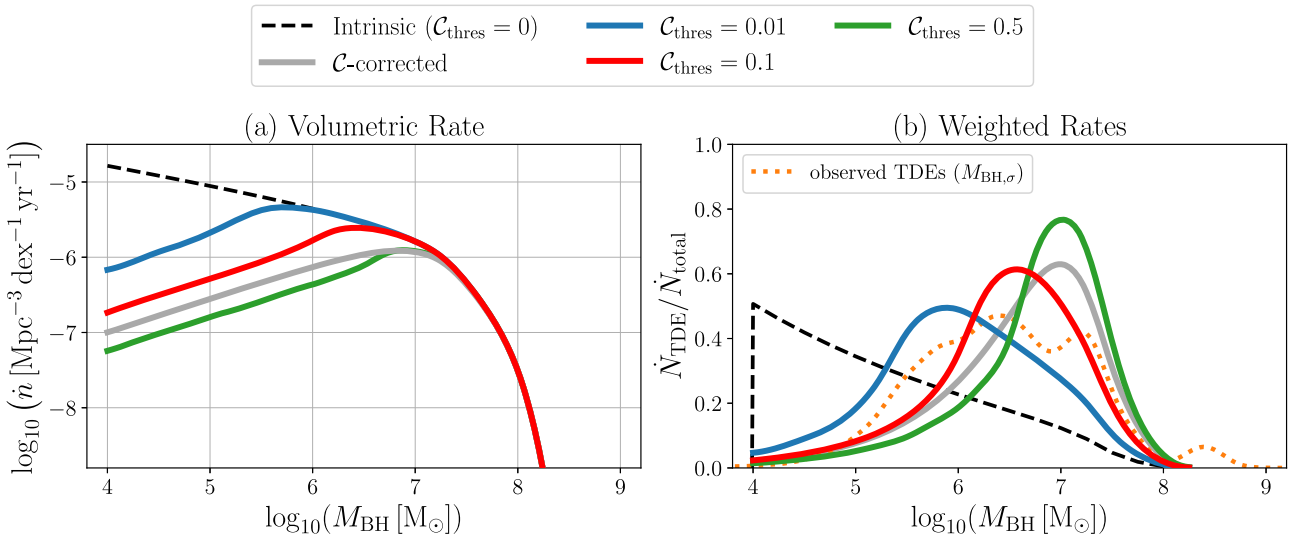

Figure 3. The intrinsic and $\mathcal{C}$-corrected volumetric TDE rates and $M_{\rm BH}$ distributions. Panel (a) shows the TDE volumetric rates as a function of $M_{\rm BH}$, with different ways of implementing the disk formation efficiency correction. Panel (b) shows how the value of $\mathcal{C}_{\rm thres}$ affects the TDE $M_{\rm BH}$ distribution. The intrinsic and observed distributions (orange dotted: $M_{\rm BH-\sigma}$), same as in Figure 1, are included for comparison. The distribution with $\mathcal{C}_{\rm thres}=0.1$ (red solid) best replicates the median of the observed TDE samples. Overall, the rate suppression around light SMBHs due to slow disk formation is evident in both plots.

centroid values at $M_{\rm BH}\approx 10^{6.5}\,M_\odot$. This suggests that current transient surveys favor the detection of TDEs with moderately prompt disk formation.

4. Distributions of TDE: Penetration Parameter and Stellar Mass

4.1. Distribution of the Penetration Parameter β

The intrinsic $\mathcal{P}(\beta)$ and $\mathcal{C}$-corrected $\mathcal{P}_\mathcal{C}(\beta)$ β probability density functions can be numerically computed respectively as

$$\frac{d\mathcal{P}}{d\beta}=\frac{1}{\beta\Gamma}\int\left(\frac{d^2\Gamma}{d\,\ln\beta\,d\,\ln m_\star}\right)d\,\ln m_\star, \tag{11a}$$

$$\frac{d\mathcal{P}_\mathcal{C}}{d\beta}=\frac{1}{\beta\Gamma_\mathcal{C}}\int\left(\frac{d^2\Gamma_\mathcal{C}}{d\,\ln\beta\,d\,\ln m_\star}\right)d\,\ln m_\star. \tag{11b}$$

We show the intrinsic β-distributions (Figure 4(a)) for three representative $M_{\rm BH}$. For $1\ll\beta\ll\beta_{\rm max}^{10\,M_\odot}$, we find $d\mathcal{P}/d\beta\propto\beta^{-2}$, which is consistent with the rate dominated by the full LC regime (see Stone & Metzger 2016). After β reaches around $\beta_{\rm max}^{0.08\,M_\odot}$ (maximal possible β for TDEs of $m_\star=0.08\,M_\odot$), low-mass stars start to plunge into the horizon, resulting in a drop in the slope. The β-distributions are cut off at $\beta_{\rm max}^{10\,M_\odot}$ when all stars undergo direct plunging. On the other side, as $\beta\to 1$, $d\mathcal{P}/d\beta$ is expected to peak owing to the additional contribution from TDEs in the diffusive regime.

The β-distributions with the $\mathcal{C}$ correction implemented are shown in Figures 4(b) and 4(c). As expected, low-β TDEs are removed, and larger $\mathcal{C}_{\rm thres}$ values generally yield higher low-β cutoffs. Adopting the nominal value of $\mathcal{C}_{\rm thres}=0.1$, we can see that for $M_{\rm BH}\lesssim 10^6\,M_\odot$, low-$\beta$ TDEs are significantly reduced. Furthermore, for IMBHs with $M_{\rm BH}\lesssim 10^4\,M_\odot(10^5\,M_\odot)$, only TDEs with $\beta\gtrsim 20(5)$ can have prompt disk formation.

The numerically obtained β-distributions in Figures 4(a) and (b) could be accurately fitted in log–log space with the following empirical formulae:

$$\left.\frac{d\mathcal{P}}{d\beta}\right|_{\rm fit}\propto\left[\left(\frac{\beta}{\beta-1}\right)^{0.1}+\left(\frac{\beta}{\beta-1}\right)^{-0.1}-2\right]\times\exp\left[-2\left(\frac{\beta}{\beta_{\rm max}^{10M_\odot}}\right)^{2.7}\right]\ \text{for}\ 1\lesssim\beta<\beta_{\rm max}^{10\,M_\odot}, \tag{12a}$$

$$\left.\frac{d\mathcal{P}_\mathcal{C}}{d\beta}\right|_{\rm fit}\propto\left[\left(\frac{\beta}{\beta-1}\right)^{0.6}+\left(\frac{\beta}{\beta-1}\right)^{-0.6}\right]\times\exp\left[-9\left(\frac{\beta}{\beta_{\rm max}^{10\,M_\odot}}\right)^{1.1}\right]\ \text{for}\ 1\lesssim\beta<\beta_{\rm max}^{10\,M_\odot}, \tag{12b}$$

which are overplotted on the numerical results. The generic form of the formulae captures the entire behavior across the full β range: the rising toward $\beta\approx 1$, the asymptotic β^{-2} proportionality (β independent) in the $1\ll\beta\ll\beta_{\rm max}^{10\,M_\odot}$ regime, and the fast exponential decay while approaching $\beta_{\rm max}^{10\,M_\odot}$, with a maximum error of 0.39 dex.

4.2. Distribution of the Disrupted Stellar Mass $m_\star$

In a similar fashion, we can calculate the intrinsic $\mathcal{P}(m_\star)$ and $\mathcal{C}$-corrected $\mathcal{P}_\mathcal{C}(m_\star)$ stellar probability density functions as

$$\frac{d\mathcal{P}}{dm_\star}=\frac{1}{m_\star\Gamma}\int\left(\frac{d^2\Gamma}{d\,\ln\beta\,d\,\ln m_\star}\right)d\,\ln\beta, \tag{13a}$$

$$\frac{d\mathcal{P}_\mathcal{C}}{dm_\star}=\frac{1}{m_\star\Gamma_\mathcal{C}}\int\left(\frac{d^2\Gamma_\mathcal{C}}{d\,\ln\beta\,d\,\ln m_\star}\right)d\,\ln\beta. \tag{13b}$$

Figure 5 shows the predicted stellar-mass distribution for a range of black hole masses. One can see that the intrinsic LC process somewhat suppresses the representation of low-mass stars in TDEs (see Pfister et al. 2022 for the explanation). The suppression is not strong unless when $M_{\rm BH}>10^7\,M_\odot$ and low-mass stars on high-β

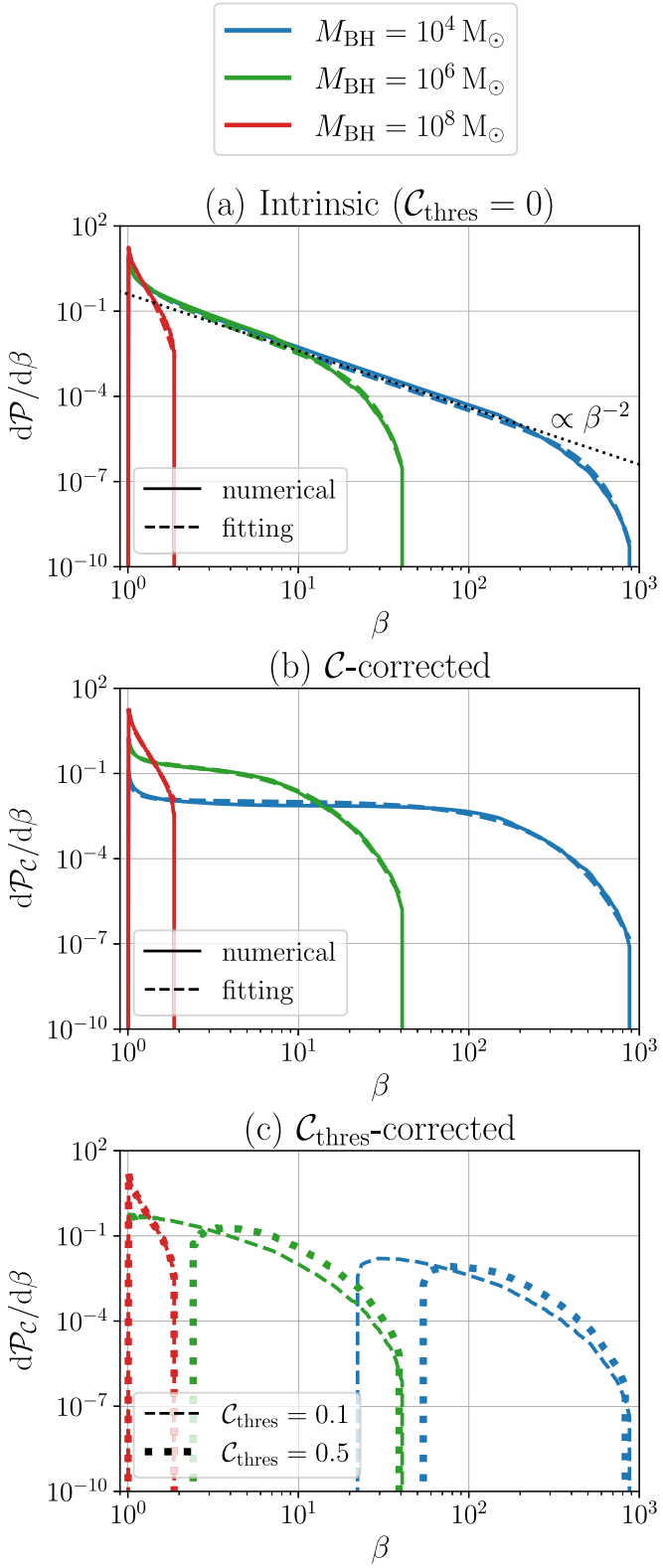

Figure 4. Numerical and empirically fitted β-distributions derived from intrinsic and $\mathcal{C}$-corrected TDE rates. Different colors indicate different $M_{\rm BH} = 10^4\,M_\odot$(blue), $10^6\,M_\odot$(green), $10^8\,M_\odot$(red). In panels (a) and (b), empirical fitting formulae of Equations (12a) and (12b) are plotted in dashed lines with their corresponding numerical results in solid lines. In panel (c), two different $\mathcal{C}_{\rm thres} = 0.1$(dashed) and 0.5 (dotted) are included.

orbits start to directly plunge. When $M_{\rm BH} \gtrsim 10^8\,M_\odot$, one can see all low-mass stars are removed.

The disk formation efficiency, however, is higher for low-mass stars and therefore leads to an enhancement of their presence in the observed TDE population. When putting all the factors together, for the majority TDE population ($M_{\rm BH} \lesssim 10^6 M_\odot$), we should still expect to observe more TDEs from low-mass stars than from the initial stellar-mass distribution.

5. Discussion and Summary

In this paper, we consider how the physics of TDE disk formation can affect their observed rates and demographics. We summarize our findings below:

1. We have systematically recalculated the host BH masses for an updated list of observed TDEs using two methods, $M_{\rm BH}$–σ and $M_{\rm BH}$–$M_{\rm gal}$, based on the observed values of σ and $M_{\rm gal}$ from previous literature. We find that the observed TDE $M_{\rm BH}$ distribution peaks between 10^6 and $10^7\,M_\odot$, which shows a drastic discrepancy when compared to the intrinsic distribution of TDE $M_{\rm BH}$ obtained using the LC dynamics and the BHMF (Figure 1).
2. We address this discrepancy by considering the efficiency of TDE disk formation ($\mathcal{C}$), which is quantified to first order as the ratio of the energy loss in the first stream self-crossing over the total energy needed to be reduced for complete circularization (Equation (5)). We find that for BHs with $M_{\rm BH} \lesssim 10^6\,M_\odot$, $\mathcal{C}$ is typically very low ($\lesssim$0.1) for typical TDEs with low β (Figure 2).
3. While applying $\mathcal{C}$ to correct the TDE rates, we naturally obtain a significant suppression of TDE rates around lighter BHs. The $M_{\rm BH}$ distribution peak can be shifted to fit the observed one when we only keep the TDEs with $\mathcal{C} \gtrsim 0.1$ (Figure 3).
4. There are a few interesting consequences induced by including the $\mathcal{C}$ correction. First, high-β TDEs are favored since they have more prompt disk formation. Therefore, the β-distribution of the TDEs with prompt disk formation is much flatter than the intrinsic one (Figure 4). We provide the fitted formulae for both the intrinsic and corrected β-distributions (Equations (12a) and 12b). Second, in most TDEs, the low-mass star population is expected to be enhanced compared to their intrinsic weight, unless when $M_{\rm BH} \gtrsim 10^7\,M_\odot$, for which low-mass stars directly plunge (Figure 5).

With the next-generation all-sky transient surveys such as the Vera Rubin Observatory, the TDE sample size will increase by tens of times, making it possible to use TDEs as probes of the demographics of massive BHs and stars in the centers of galaxies. In this work, using first principles, we have demonstrated that it is important to understand how physical processes in TDEs, such as how promptly the debris forms a disk, can significantly impact the distributions of $M_{\rm BH}$ and $m_\star$ obtained from TDE observations.

It is important to stress that our study aims at providing one important link narrowing the gap between the intrinsic and the observed TDE rates and demographics. There can be other factors that are affecting the observed TDE $M_{\rm BH}$ distribution, such as dust obscuration/reddening and the sensitivity and bias of the instruments. Also, the chance of detecting a TDE necessarily depends on its luminosity (in monochromatic bands), and more studies of TDE emission processes are required for understanding how the luminosity links to $M_{\rm BH}$ and other parameters. Moreover, we acknowledge that the low-mass end of the BHMF still has large

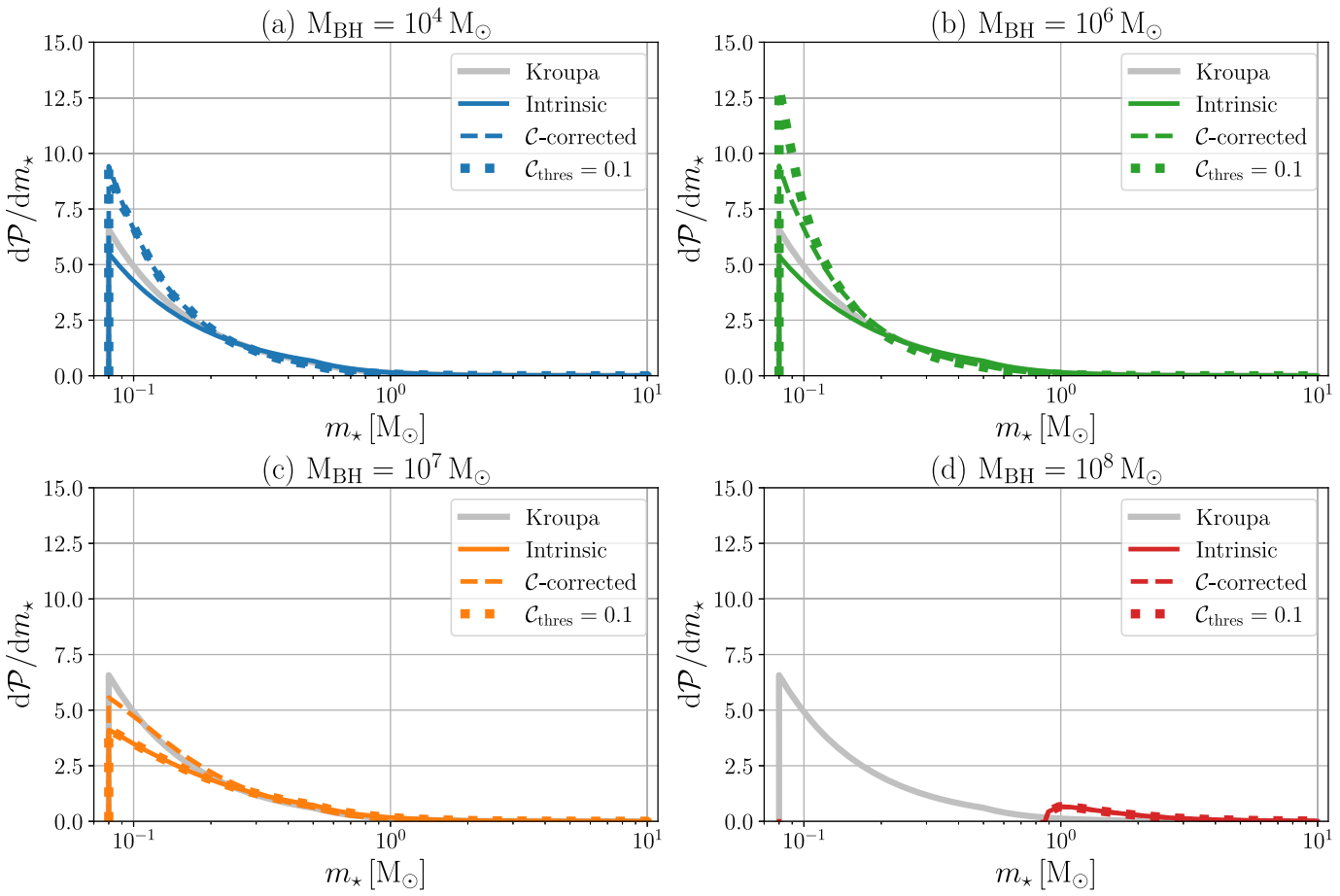

Figure 5. The stellar-mass probability density functions in TDEs before and after the correction with $\mathcal{C}$. For four distinct $M_{BH} = 10^4\,M_\odot$ (blue), $10^6\,M_\odot$ (green), $10^7\,M_\odot$ (orange), and $10^8\,M_\odot$ (red), we show the intrinsic (solid), $\mathcal{C}$-corrected (dashed), and $\mathcal{C}_{thres} = 0.1$ case (dotted) stellar-mass distributions in TDEs. The Kroupa initial mass function is plotted for comparison (gray solid). Low-mass stars have a lower intrinsic presentation in TDEs due to a combination of the LC physics as well as their direct plunge when M_{BH} is large. For TDEs with $M_{BH} \gtrsim 10^8\,M_\odot$, there exists a cutoff of low-mass stars. For TDEs with $M_{BH} \lesssim 10^6\,M_\odot$, the $\mathcal{C}$-correction can overcompensate for the suppression of low-mass stars.

uncertainties, which directly links to the rates of TDEs around low-mass SMBHs. Eventually, comprehensive forward modeling including all these factors will be needed to bring theory and observation together.

We thank Alex Dittmann, Tiara Hung, Cole Miller, Brenna Mockler, and Sjoert van Velzen for useful comments and discussions. The authors acknowledge the support from the Hong Kong Research Grants Council (HKU27305119 and HKU17304821) and the National Natural Science Foundation of China (HKU12122309).

Appendix A
TDE Host Black Hole Masses

In this appendix, we present the criteria used to select the likely TDEs among the many other TDE candidates as our observed sample and further elaborate on the properties of both the host BH mass and luminosity distributions we find.

A.1. TDE Selection and Black Hole Mass Calculation

Among a total of a hundred or so detected TDE candidates, we select 65 TDEs to include in our analysis. The chosen TDE candidates are listed in Table A1 with some of their host-galaxy properties. Detailed criteria for the selection of TDE candidates are as follows.

1. Categorized as a possible/likely/confirmed TDE in at least two of the following references: Auchettl et al. (2017), Wevers et al. (2017, 2019), French et al. (2020), and van Velzen et al. (2021).
2. All TDEs in Table A1 of Gezari (2021)
3. All ZTF TDEs (van Velzen et al. 2021)

Also, we intentionally exclude all likely partial TDEs, e.g., iPTF-16fnl and PS1-11af, from our sample because our calculation only applies to fully disrupted stars.

We also obtain the TDE host black hole mass with two different methods. We either derive their M_{BH} all using the $M_{BH}-\sigma$ relation (Merritt & Ferrarese 2001):

$$\log_{10}\left(\frac{M_{BH,\sigma}}{M_\odot}\right) = \log_{10} \times \left[10^8 \cdot (1.48 \pm 0.24)\left(\frac{\sigma}{200\ \mathrm{km\ s^{-1}}}\right)^{4.65\pm0.48}\right] \quad \text{(A1)}$$

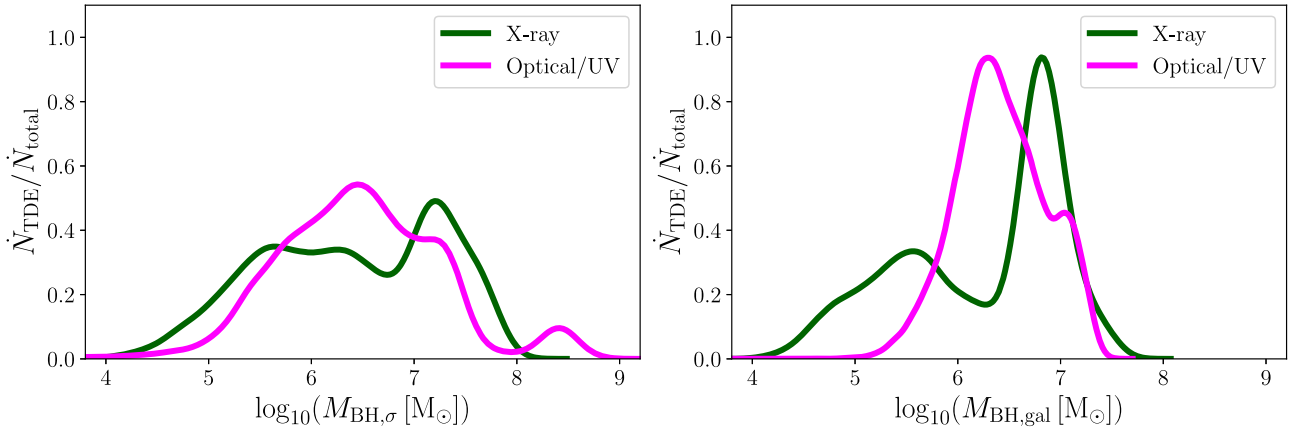

Figure A1. TDE host $M_{\rm BH}$ distribution for X-ray-strong or optical/UV-strong TDEs. The two colored curves in Figure 1 are further decomposed into two groups: optical/UV strong (magenta) or X-ray strong (green). The optical/UV TDE $M_{\rm BH}$ distribution still peaks somewhere between 10^6 and $10^7 M_\odot$, while that of the X-ray TDEs exhibits a double peak behavior.

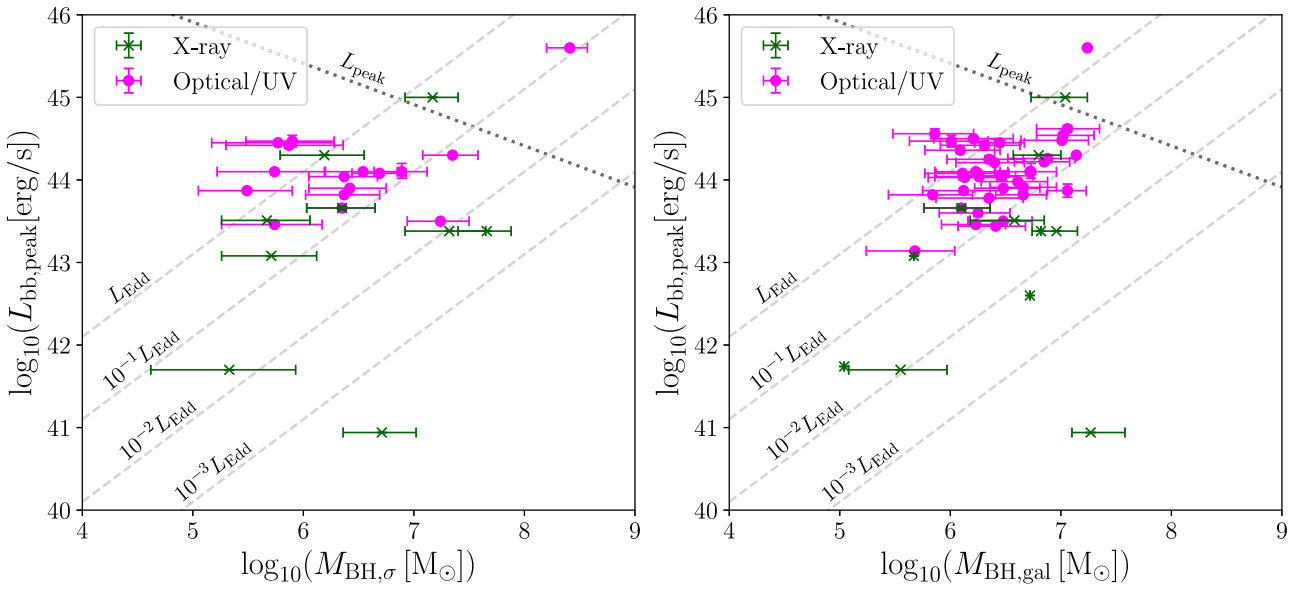

Figure A2. TDE peak luminosity $L_{\rm bb,peak}$ vs. $M_{\rm BH}$ from Table A1 (modified from Figure 16 Hung et al. 2017). The optical/UV-strong TDEs are marked by magenta dots and the X-ray strong by green crosses, with the horizontal line showing the error bar of $M_{\rm BH}$. The dashed lines correspond to four different Eddington ratios, while the dotted line shows the $\dot{M}_{\rm peak} \propto M_{\rm BH}^{-1/2}$ proportionality relation derived in Guillochon & Ramirez-Ruiz (2013), their Equation (A1), with $m_\star = 1 M_\odot$, $\gamma = 4/3$, $\beta = 1$, and radiative efficiency $\eta = 0.1$. We find here that some TDEs have peak luminosity exceeding the Eddington limits of their host SMBHs: ASASSN-14ae, ASASSN-15lh, ASASSN-15oi, ASASSN-19dj, AT 2018hyz, AT 2018lna, AT 2019meg, PS1-10jh, and SDSS J1323–4827. Overall, no apparent correlation is found between $L_{\rm bb,peak}$ and $M_{\rm BH}$.

or using the $M_{\rm BH}$–$M_{\rm gal}$ relation (Reines & Volonteri 2015):

$$\log_{10}\left(\frac{M_{\rm BH,gal}}{M_\odot}\right) = (7.45 \pm 0.08) + (1.05 \pm 0.11)\log_{10}\left(\frac{M_{\rm gal}}{10^{11}\,M_\odot}\right). \quad \text{(A2)}$$

The derived BH masses as well as other quantities such as the peak luminosity (assuming blackbody emission) are listed in Table A1. The error bar of each derived $M_{\rm BH}$ is computed by modeling a Gaussian distribution using the measurement errors of the velocity dispersion σ and the total galaxy mass $M_{\rm gal}$, with the curve-fitting 1σ error of Equations (A1) and (A2). The Gaussian distributions peak at the mean value $\log_{10}\bar{M}_{\rm BH}$ with standard deviation $s = (\log_{10}M_{\rm BH}^{\rm up} - \log_{10}M_{\rm BH}^{\rm low})/2$.

We plot the $M_{\rm BH}$ distribution of all TDE samples obtained from either method in Figure 1. The overall trends are similar, but the detailed shapes of the two distributions are somewhat different from each other. The main reason for this the that for many TDEs we lack measurements of σ. We further separate between the optical/UV-strong (magenta) and X-ray-strong (green) TDE samples in Figure A1. It can be clearly seen that the X-ray-strong TDEs have a bimodal distribution in $M_{\rm BH}$, but we believe that this effect is primarily due to the limited sample size of this TDE category. Thus, shifting of the distribution, perhaps reducing to a single peak, is highly likely when more are observed. Another possibility is related to the TDE

emission mechanism in different wave bands, which deserves extensive study.

A.2. TDE Luminosity Distribution

In Figure A2 we plot the TDE peak luminosity $L_{\rm bb,peak}$ distribution against $M_{\rm BH}$. One might expect that the luminosity should generally increase somewhat linearly with $M_{\rm BH}$ if the Eddington limit is the primary factor determining $L_{\rm bb,peak}$ (Kochanek 2016); however, here one could barely see any trend of $L_{\rm bb,peak}$ as a function of $M_{\rm BH}$. We note that the currentl sample size is limited and the range of observed TDE $M_{\rm BH}$ is narrow, which forbid us from drawing any conclusion on whether or how much the Eddington limit is playing a role in determining the luminosity of TDEs. We also recognize that there are further layers of complications like the flux limits of different instruments (van Velzen 2018) and dust obscuration from host galaxies (Roth et al. 2018). The number of detected TDEs of a given transient survey has a nonlinear dependency on its effective flux limit, and their limits could be used to derive the maximum redshifts each survey are capable of reaching given a peak luminosity. To stimulate a detection, not only should the event peak luminosity surpass the survey sensitivity in specific wave bands, but it also has to have significant contrast compared with the flux of its host galaxy. Even worse, the effects of dust (neutral gas) at optical/UV (X-ray) wavelengths in the host galaxies would obstruct our observation and selection capability. Hence the observed TDE samples unavoidably suffer from further external observational bias.

Appendix B
Derivations of Energy Dissipation in Stream–Stream Collisions

We summarize the results in Dai et al. (2015) on debris stream self-crossing and disk formation in TDEs. The most bound debris has a specific binding energy of

$$E_{\rm mb}=\frac{1}{2}v_T^2-\frac{GM_{\rm BH}}{r_T-r_\star}\approx-\frac{GM_{\rm BH}r_\star}{r_T^2}\ \text{for}\ r_T\gg r_\star, \tag{B1}$$

where v_T is the orbital velocity at the tidal radius r_T and $r_\star$ is the stellar radius. Furthermore, the semimajor axis and eccentricity of this orbit are $a_{\rm mb}=r_T^2/2r_\star$ and $e_{\rm mb}=1-r_p/a_{\rm mb}\approx 1-2(m_\star/M_{\rm BH})^{1/3}/\beta$, respectively, where r_p is the pericenter distance and β is the penetration parameter. The stellar debris orbits around a Schwarzschild SMBH goes through apsidal precession. We approximate the process using an instantaneous shift at r_p with an angle of

$$\phi=\frac{6\pi GM_{\rm BH}}{c^2a(1-e^2)}. \tag{B2}$$

Using these, the intersection radius and the angle of the incoming and outgoing debris stream are calculated to be

$$R_I(M_{\rm BH},\beta,m_\star)=\frac{(1+e_{\rm mb})r_T}{\beta[1-e_{\rm mb}\cos(\phi/2)]}, \tag{B3}$$

$$\cos\Theta=\frac{1-2e_{\rm mb}\cos(\phi/2)+e_{\rm mb}^2\cos\phi}{1-2e_{\rm mb}\cos(\phi/2)+e_{\rm mb}^2}. \tag{B4}$$

Assuming totally inelastic collision of the debris streams and using the conservation of momentum, the debris speeds before collision v_i and after collision v_f are related as

$$v_f=v_i\cos(\Theta/2), \tag{B5}$$

where v_i can be calculated using the conservation of energy:

$$-\frac{GM_{\rm BH}}{2a_{\rm mb}}=-\frac{GM_{\rm BH}}{R_I}+\frac{1}{2}v_i^2. \tag{B6}$$

We can then obtain the specific energy loss in the first self-crossing for the calculation of disk formation efficiency:

$$\Delta E_{\rm first}(M_{\rm BH},\beta,m_\star)=\left|\frac{1}{2}v_f^2-\frac{1}{2}v_i^2\right|=\frac{1}{2}v_i^2\sin^2(\Theta/2). \tag{B7}$$

Appendix C
Supplementary Information on Loss Cone Dynamics

In classical LC calculations, the commonly used variables are defined as the specific energy E, the specific angular momentum J, and the scaled dimensionless angular momentum $\mathcal{R}=J^2/J_C^2$, where J_C is the specific angular momentum of a circular orbit. The orbital period $P(E)$ and the stellar distribution function $f(E,\mathcal{R})$ can be derived using these variables (e.g., Merritt 2013; Stone & Metzger 2016). Considering f outside of the disruption zone ($\mathcal{R}>\mathcal{R}_{\rm LC}$), where $\mathcal{R}_{\rm LC}$ is defined as the critical angular momentum at which stars would inevitably be tidally disrupted if their $\mathcal{R}<\mathcal{R}_{\rm LC}$:

$$\lim_{E\ll GM_{\rm BH}/r_T}\mathcal{R}_{\rm LC}(E,M_{\rm BH},m_\star)\approx\frac{4Er_T}{GM_{\rm BH}}\ll 1, \tag{C1}$$

it could be deduced that the mean $\mathcal{R}$-integrated distribution function has the limiting behavior of $\mathcal{R}\approx 1$:

$$\bar{f}(E)=\frac{\int_{\mathcal{R}_{\rm LC}}^1 f(E,\mathcal{R})d\mathcal{R}}{\int_{\mathcal{R}_{\rm LC}}^1 d\mathcal{R}}\approx f(E,1). \tag{C2}$$

The limit $E\ll GM_{\rm BH}/r_T$ is used here because the majority of stars approach in elliptical orbits with semimajor axes $r_a\gg r_T$.

The rate calculation in this work follows closely that in Pfister et al. (2022), who have shown in detail the derivations of TDE rate by assuming:

1. A stellar population described by the Kroupa stellar-mass function of the MS stars (Kroupa 2001):

$$\frac{\phi(m_\star)}{M_\odot^{-1}}=\phi_0\begin{cases}\left(\frac{m_\star}{0.5\,M_\odot}\right)^{-1.3} & \text{for } 0.08\,M_\odot\leqslant m_\star\leqslant 0.5\,M_\odot\\ \left(\frac{m_\star}{0.5\,M_\odot}\right)^{-2.3} & \text{for } 10\,M_\odot\leqslant m_\star\leqslant 0.5\,M_\odot\\ 0 & \text{else}\end{cases}. \tag{C3}$$

   The normalization constant ϕ_0 ensures that $\int_0^\infty\phi(m_\star)dm_\star=1$.
2. A power-law stellar density profile near the SMBH:

$$\rho(r)=\rho_0\left(\frac{r}{r_{\rm inf}}\right)^{-\alpha}, \tag{C4}$$

   where $r_{\rm inf}$ is the SMBH radius of influence, defined as the

radius where $2\pi\int_0^{r_{\rm inf}} u^2\rho(u)du = M_{\rm BH}$. We assume an isothermal profile ($\alpha = 2$), which leads to

$$r_{\rm inf} = \frac{GM_{\rm BH}}{2\sigma^2}, \tag{C5}$$

where σ, the velocity dispersion of the galaxy, is constant in the case of an isothermal sphere.

3. An $M_{\rm BH}$–σ BH mass scaling relation by Merritt & Ferrarese (2001):

$$\sigma = 200\left(\frac{M_{\rm BH}}{(1.48\pm0.24)\times10^8\,M_\odot}\right)^{1/(4.65\pm0.48)}\ {\rm km\ s^{-1}}. \tag{C6}$$

Based on the above assumptions, the differential TDE rate as a function of ($M_{\rm BH}$, β, $m_\star$) after careful consideration of stellar diffusion through two-body gravitational scattering is given by Pfister et al. (2022) and Strubbe (2011)

$$\mathcal{G}(E, M_{\rm BH}, \beta, m_\star) = \frac{f(E)}{1 + q^{-1}\xi\ln(\mathcal{R}_{\rm LC}^{-1})} \times\left[1 - 2\sum_{m=1}^{\infty}\frac{e^{-\alpha_m^2 q/4}}{\alpha_m}\frac{J_0(\alpha_m\beta^{-1/2})}{J_1(\alpha_m)}\right], \tag{C7}$$

$$\xi = 1 - 4\sum_{m=1}^{\infty}\frac{e^{-\alpha_m^2 q/4}}{\alpha_m^2}, \tag{C8}$$

$$q(E, M_{\rm BH}, m_\star) = \frac{P(E)\bar{\mu}(E, \langle m_\star^2\rangle^{1/2})}{\mathcal{R}_{\rm LC}}, \tag{C9}$$

where q and $\bar{\mu}$ are the LC filling factor and orbit-averaged diffusion coefficient respectively. J_0 and J_1 are the Bessel functions of the first kind of order zero and one, respectively, and α_m is the mth zero of J_0.

By assuming a power-law stellar density profile around the SMBH, the stellar distribution function f and the LC refilling factor q could be computed analytically rather than numerically in the usually complicated scenarios. The expressions are as follows (Magorrian & Tremaine 1999; Strubbe 2011; Merritt 2013; Stone & Metzger 2016):

$$f(E) = (2\pi\sigma_{\rm inf}^2)^{-3/2}\frac{\rho_0}{\langle m_\star\rangle}\frac{\gamma(\alpha+1)}{\gamma(\alpha-1/2)}\left(\frac{E}{\sigma_{\rm inf}^2}\right)^{\alpha-3/2}, \tag{C10}$$

$$q(E, m_\star) = \nu\left(\frac{E}{\sigma_{\rm inf}^2}\right)^{\alpha-4}, \tag{C11}$$

$$\nu(m_\star) = \frac{8\sqrt{\pi}}{3}(3-\alpha)\frac{\gamma(\alpha+1)}{\gamma(\alpha-1/2)}\left[\frac{5}{32(\alpha-1/2)} + \frac{3I_B(1/2,\alpha) - I_B(3/2,\alpha)}{4\pi}\right]\left(\frac{G\langle m_\star^2\rangle}{\sigma_{\rm inf}^2 r_T}\right)\ln\Lambda, \tag{C12}$$

where $\sigma_{\rm inf} = \sqrt{GM_{\rm BH}/r_{\rm inf}}$ is the velocity dispersion at the radius of influence of the BH with mass $M_{\rm BH}$, $\ln\Lambda = \ln(0.4M_{\rm BH}/\langle m_\star\rangle)$ is the Coulomb logarithm, γ is the Euler–Gamma function, and I_B is an expression defined in Strubbe (2011):

$$I_B\left(\frac{n}{2},\alpha\right) = \int_0^1 t^{-\frac{n+1}{2}}(1-t)^{3-\alpha}B\left(t,\frac{n}{2},\alpha-\frac{1}{2}\right)dt, \tag{C13}$$

where $B\left(t,\frac{n}{2},\alpha-\frac{1}{2}\right)$ is the incomplete Euler–Beta function.

Initially, the orbit-averaged diffusion coefficient $\bar{\mu}$ in Equation (C9) should be a function of the specific energy of the disrupted star E, the mass of the star $m_\star$, and the mass of a background star $m_{\rm bg}$, assuming a monochromatic distribution of stellar mass. Magorrian & Tremaine (1999) show that the derived rate using a stellar population is the same as a monochromatic distribution of stellar masses of $m_{\rm bg} = \langle m_\star^2\rangle^{1/2}$, where $\langle m_\star^2\rangle = \int m_\star^2\phi(m_\star)dm_\star$. Pfister et al. (2022) ignore the effect of mass segregation in which this approximation is no longer valid when stellar distribution becomes a function of position.

In order to apply a semianalytical calculation of TDE rate based on LC dynamics onto a general galaxy system, numerous assumptions and approximations have to be made. For a more accurate estimate of the TDE rate in a specific galaxy, characteristics of the galaxy, such as the stellar density profile and the host BH mass, shall not simply be assumed to follow Equations (C3), (C4), and (C6).

Appendix D
Effect of Uncertainty in the Black Hole Mass Function

One might suspect that the suppression of the TDE host $M_{\rm BH}$ demographics at the low-mass end could result from the large uncertainty of BHMF at $M_{\rm BH}\lesssim10^6\,M_\odot$. For example, the 2σ uncertainty regions in Figure 2 of Gallo & Sesana (2019) indicate that the volumetric density of SMBHs might increase or decrease with decreasing $M_{\rm BH}$ in this mass range. In the lower-mass end ($M_{\rm BH}\sim10^{4-5}\,M_\odot$), the maximum spread is about $^{+0.5{\rm dex}}_{-0.8{\rm dex}}$.

We calculate the corresponding TDE volumetric rates and their host $M_{\rm BH}$ distributions using the upper and lower 95% confidence regions in Gallo & Sesana (2019) (Figure D1). The overall shapes of the intrinsic and the $\mathcal{C}$-corrected distributions still remain somewhat similar to that of Figure 3, despite some boost (upper 2σ) or further suppression (lower 2σ) at the low-mass ends. It can be seen that even with the lower 2σ BHMF, the intrinsic TDE BHH mass distribution still has too much weight toward the lower side. In order to shift the theoretical

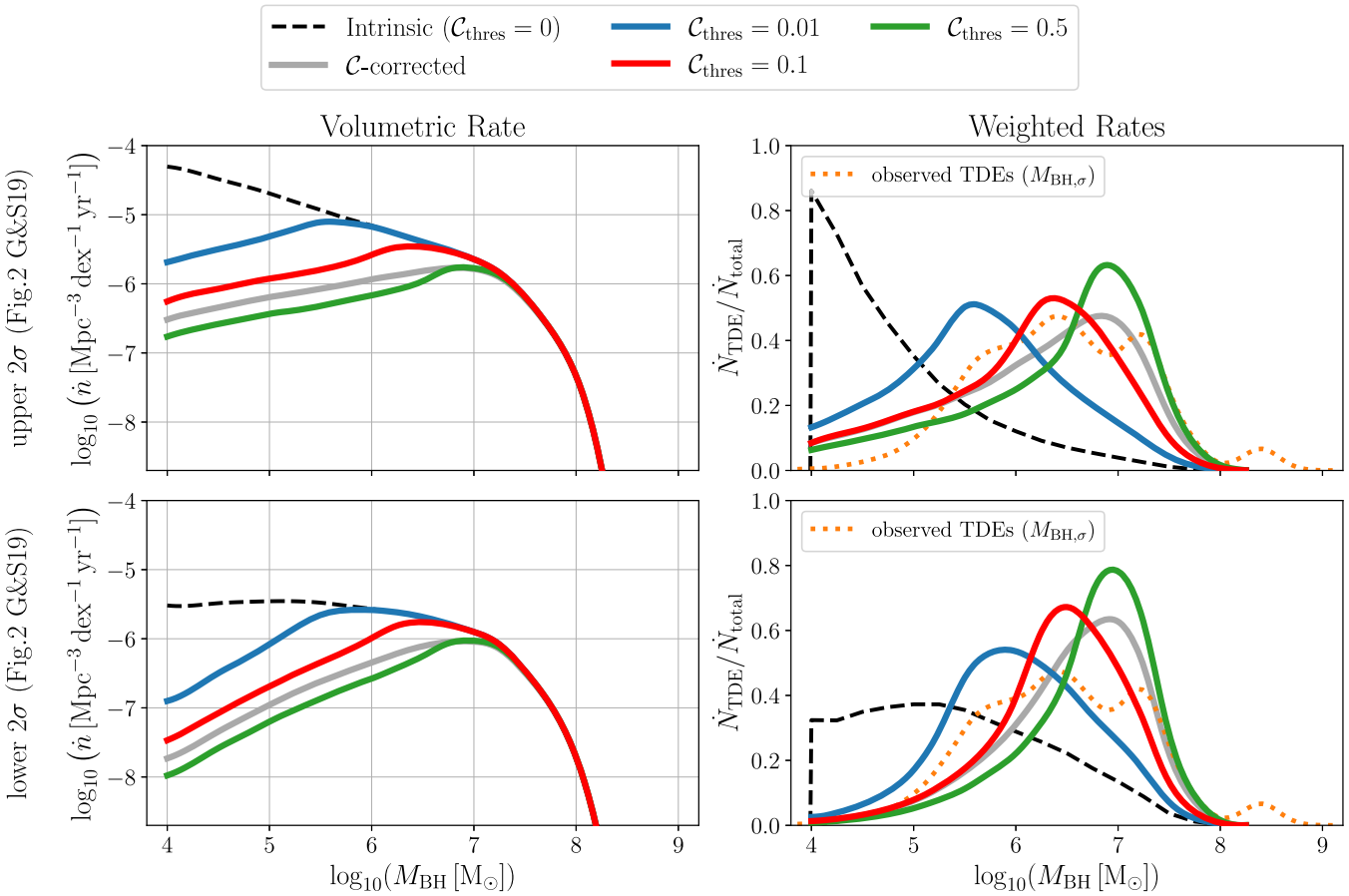

Figure D1. Regenerated Figure 3 using the 95% confidence regions of the BHMF in Figure 2 in Gallo & Sesana (2019). The upper (lower) panel corresponds to using the BHMF's upper (lower) margin in the light yellow areas of Gallo & Sesana (2019) Figure 2. The distributions with $\mathcal{C}_{\rm thres} = 0.1$ (red solid) still best replicate the median of the observed TDE samples. The rate suppression around light SMBHs due to slow disk formation is more dominant than that by the lower 2σ of the unconstrained BHMF.

distributions to peak at that of the observed, $\mathcal{C}_{\rm thres} \approx 0.1$ is still needed in both cases.

ORCID iDs

Thomas Hong Tsun Wong https://orcid.org/0000-0001-5570-0926

References

Auchettl, K., Guillochon, J., & Ramirez-Ruiz, E. 2017, ApJ, 838, 149
Bonnerot, C., & Lu, W. 2020, MNRAS, 495, 1374
Bonnerot, C., & Stone, N. C. 2021, SSRv, 217, 16
Dai, J. L., Lodato, G., & Cheng, R. 2021, SSRv, 217, 12
Dai, L., Escala, A., & Coppi, P. 2013, ApJL, 775, L9
Dai, L., McKinney, J. C., & Miller, M. C. 2015, ApJL, 812, L39
French, K. D., Wevers, T., Law-Smith, J., Graur, O., & Zabludoff, A. I. 2020, SSRv, 216, 32
Gallo, E., & Sesana, A. 2019, ApJL, 883, L18
Gezari, S. 2021, ARA&A, 59, 21
Graur, O., French, K. D., Zahid, H. J., et al. 2018, ApJ, 853, 39
Guillochon, J., & Ramirez-Ruiz, E. 2013, ApJ, 767, 25
Guillochon, J., & Ramirez-Ruiz, E. 2015, ApJ, 809, 166
Hung, T., Gezari, S., Blagorodnova, N., et al. 2017, ApJ, 842, 29
Kesden, M. 2012, PhRvD, 85, 024037
Kippenhahn, R., & Weigert, A. 1990, Stellar Structure and Evolution (New York: Springer)
Kochanek, C. S. 1994, ApJ, 422, 508
Kochanek, C. S. 2016, MNRAS, 461, 371
Komossa, S., Zhou, H., Wang, T., et al. 2008, ApJL, 678, L13
Kroupa, P. 2001, MNRAS, 322, 231
Law-Smith, J., Guillochon, J., & Ramirez-Ruiz, E. 2019, ApJL, 882, L25
Law-Smith, J. A. P., Coulter, D. A., Guillochon, J., Mockler, B., & Ramirez-Ruiz, E. 2020, ApJ, 905, 141
Liptai, D., Price, D. J., Mandel, I., & Lodato, G. 2019, arXiv:1910.10154
Lu, W., & Bonnerot, C. 2020, MNRAS, 492, 686
Magorrian, J., & Tremaine, S. 1999, MNRAS, 309, 447
Merritt, D. 2013, CQGra, 30, 244005
Merritt, D., & Ferrarese, L. 2001, in ASP Conf. Ser. 249, The Central Kiloparsec of Starbursts and AGN: The La Palma Connection, ed. J. H. Knapen (San Francisco, CA: ASP), 335
Mockler, B., Guillochon, J., & Ramirez-Ruiz, E. 2019, ApJ, 872, 151
Pfister, H., Bar-Or, B., Volonteri, M., Dubois, Y., & Capelo, P. R. 2019, MNRAS, 488, L29
Pfister, H., Toscani, M., Wong, T. H. T., et al. 2022, MNRAS, 510, 2025
Pfister, H., Volonteri, M., Dai, J. L., & Colpi, M. 2020, MNRAS, 497, 2276
Piran, T., Svirski, G., Krolik, J., Cheng, R. M., & Shiokawa, H. 2015, ApJ, 806, 164
Rees, M. J. 1988, Natur, 333, 523
Reines, A. E., & Volonteri, M. 2015, ApJ, 813, 82
Roth, N., Mushotzky, R., Gezari, S., & van Velzen, S. 2018, BAAS, 231, 405.03
Roth, N., Rossi, E. M., Krolik, J., et al. 2020, SSRv, 216, 114
Roth, N., van Velzen, S., Cenko, S. B., & Mushotzky, R. F. 2021, ApJ, 910, 93
Ryu, T., Krolik, J., & Piran, T. 2020a, ApJ, 904, 73
Ryu, T., Krolik, J., Piran, T., & Noble, S. C. 2020b, ApJ, 904, 98
Saxton, R., Komossa, S., Auchettl, K., & Jonker, P. G. 2020, SSRv, 216, 85
Shankar, F., Bernardi, M., Sheth, R. K., et al. 2016, MNRAS, 460, 3119
Shiokawa, H., Krolik, J. H., Cheng, R. M., Piran, T., & Noble, S. C. 2015, ApJ, 804, 85

Stone, N. C., & Metzger, B. D. 2016, MNRAS, 455, 859
Stone, N. C., Vasiliev, E., Kesden, M., et al. 2020, SSRv, 216, 35
Strubbe, L. E. 2011, PhD thesis, University of California, Berkeley
Ulmer, A. 1998, in AIP Conf. Ser. 431, Accretion Processes in Astrophysical Systems: Some like it hot! - eigth AstroPhysics Conf., ed. AstroPhysics (Melville, NY: AIP), 141
van Velzen, S. 2018, ApJ, 852, 72
van Velzen, S., Holoien, T. W. S., Onori, F., Hung, T., & Arcavi, I. 2020, SSRv, 216, 124
van Velzen, S., Gezari, S., Hammerstein, E., et al. 2021, ApJ, 908, 4
Wang, J., & Merritt, D. 2004, ApJ, 600, 149
Wevers, T., van Velzen, S., Jonker, P. G., et al. 2017, MNRAS, 471, 1694
Wevers, T., Stone, N. C., van Velzen, S., et al. 2019, MNRAS, 487, 4136